This article has been accepted for publication in IEEE Transactions on Energy Conversion. This is the author's version which has not been fully edited and content may change prior to final publication. Citation information: DOI 10.1109/TEC.2022.3206795

Real-World 20-Hz IBR Subsynchronous Oscillations: Signatures and Mechanism Analysis

Lingling Fan, *Fellow, IEEE*, Zhixin Miao, *Senior Member, IEEE*, Shahil Shah, *Senior Member, IEEE*, Yunzhi Cheng, *Senior Member, IEEE*, Jonathan Rose, *Senior Member, IEEE*, Shun-Hsien Huang, *Senior Member, IEEE*, Bikash Pal, *Fellow, IEEE*, Xiaorong Xie, *Senior Member, IEEE*, Nilesh Modi, *Senior Member, IEEE*, Song Wang, *Senior Member, IEEE*, Songzhe Zhu *Senior Member, IEEE*

***Abstract*—This paper provides analyses of subsynchronous oscillations associated with solar photovoltaics (PVs) observed in real world. All have oscillation frequencies at approximately 20 Hz in voltage and current magnitudes. On the other hand, in phase voltage and current, the oscillations show very different signatures. Through constructing simplified linear models and conducting sensitivity analysis, we are able to associate dynamic phenomena with the underlying mechanism and speculate the possible causes of the 20-Hz oscillations. The analysis results have all been validated via simulation results from electromagnetic transient (EMT) test beds constructed in MATLAB/Simscape.**

***Index Terms*—Inverter-based resources, weak grids, subsynchronous oscillations.**

I. Introduction

FUNDAMENTAL understanding on inverter-based resource (IBR) subsynchronous oscillations (SSO) is imperative as high penetrations of IBRs lead to distinct dynamic phenomena. One particular phenomenon is sideband oscillations, which has also been observed in a real-world event associated with STATCOM in weak grid occurred in China Southern Grid in 2017 [1]. In phase current measurements, both 2.5-Hz and 97.5-Hz oscillations are observed. Classification of traditional power grid stability is used to treating those two oscillations as of different time scales: slow or fast [2]. On the other hand, these two components are associated with the same 47.5-Hz oscillation mode observed in the *dq* frame. Similarly, for IBR related dynamics, we can no longer separate slow and fast dynamics. Rather, wideband dynamics are to be dealt with.

The goal of this paper is to fill two gaps in our understanding. *First*, the paper provides the possible causes of three real-world IBR SSOs at 20-Hz range observed in Hydro One [3], South Australia [4], and Dominion Energy [5]. The three events all manifest $\sim$ 20 Hz oscillations in voltage root mean square (RMS) measurements. On the other hand, the signatures in phase current measurement data are very different, indicating different mechanisms. Studying those events helps to provide a better understanding on wideband IBR dynamics. *Second*, this paper will also provide a better understanding regarding IBR SSO's manifestation in measurements by examining the critical signatures in both instantaneous voltage/current and RMS measurements. Such effort is lacking in the current literature.

It has to be mentioned that none of the authors has information regarding any solar PV inverter's control information. The lack of a known model of a solar PV inverter presents an intellectual challenge on mechanism analysis. Nevertheless, data from 19 IBR SSO events have been collected in our previous efforts summarized in a task force paper [6]. In the current paper, the three 20-Hz oscillation events are singled out and the characteristics of the event data are analyzed and presented.

Our study approach is to build a computer simulation test bed, tune the test bed parameters to create oscillations, and find those that exhibit similar characteristics of the real-world event data. We also derive a linear model, examine frequency responses of the system as well as eigenvalue loci to understand the causes of oscillations.

A test bed consisting of a single voltage source converter (VSC) representing an IBR connected to a grid with shunt compensation has been constructed. This grid representation is based on the data of a real-world distribution system with 30-MW solar PV integrated [3]. In majority of the latest research in stability investigation, shunt compensation has not been considered and the grid is represented as a voltage source behind a pure reactance for simplicity. See e.g., [7]–[9]. In this research, we demonstrate that shunt compensation indeed influences certain types of oscillations significantly.

The investigation is based on a specific grid-following control (GFL) with proportional resonant (PR) current control implemented in a static frame. It leads to speculation of possible causations, e.g., slow current control, insufficient damping of PLL, and the interaction of PLL and shunt compensation. These findings may also be applicable to a GFL with dq-frame-based proportional integral (PI) current control. This is because that while there are subtle differences, GFL inverters share key common features in the critical control structure. For example, GFLs all use PLLs for synchronization. And GFLs use outer

This project is supported in part by US Department of Energy SETO DE-EE-0008771. L. Fan, Z. Miao are with the Department of Electrical Engineering, University of South Florida, Tampa, FL, 33620 (email: {linglingfan, zmiao}@usf.edu). S. Shah is with National Renewable Energy Lab, CO, USA (email: Shahil.Shah@nrel.gov). Y. Cheng, J. Rose, S. Huang are with ERCOT, TX USA (emails: {Yunzhi.Cheng, Jonathan.Rose, Shun-Hsien.Huang}@ercot.com}). B. Pal is with Imperial College, UK (email: b.pal@imperial.ac.uk). X. Xie is with the State Key Laboratory of Power System, Department of Electrical Engineering, Tsinghua University, Beijing 100080, China (e-mail: xiexr@tsinghua.edu.cn). N. Modi is with AEMO, Australia (email: nilesh.modi@aemo.com.au). S. Wang is with PacifiCorp (email: Song.Wang@pacificorp.com). S. Zhu is with GridBright (email: songzhe.zhu@gridbright.com).

© 2022 IEEE. Personal use is permitted, but republication/redistribution requires IEEE permission. See https://www.ieee.org/publications/rights/index.html for more information.
Authorized licensed use limited to: University of South Florida. Downloaded on October 29,2022 at 18:32:03 UTC from IEEE Xplore. Restrictions apply.

This article has been accepted for publication in IEEE Transactions on Energy Conversion. This is the author's version which has not been fully edited and content may change prior to final publication. Citation information: DOI 10.1109/TEC.2022.3206795

controls to generate current orders while inner current controls to track orders. The outer control bandwidth is much slower compared to the inner control bandwidth.

The remainder of the paper consists of four parts: description of real-world observation (time-series data and/or frequency spectrum data), the test bed and the linear model representation, mechanism analysis results and EMT test bed simulation results, and conclusions.

II. Real-world IBR SSO

A. Hydro One 20-Hz Oscillations

Hydro One observed 20-Hz weakly damped oscillations in voltage RMS measurements at a 44-kV distribution feeder upon switching in a 30-MVAr capacitor [3]. This feeder has three 10-MVA solar PV plants connected to the utility substation through a 30-km feeder. The fault level at the 44 kV point of common coupling (PCC) is approximately 120 MVA. Viewed from the PCC bus, the short circuit ratio (SCR) is 4.

For the instantaneous phase current, besides the fundamental frequency component at 60 Hz, there is also an 80-Hz component. Fig. 1(a) and (b) present the recorded instantaneous current and RMS voltage. Fast Fourier transform (FFT) analysis of the phase current (shown in Fig. 1(c)) shows that the 80-Hz component is predominant and has a magnitude close to 75% of the fundamental component.

One more thing to be noticed is that the oscillations were more obvious at light PV power output in the early mornings. This is a characteristic very different from many oscillations observed in weak grids. These oscillations become worse if power output is higher, e.g., the 4-Hz Texas oscillations associated with a type-4 wind farm [10].

Hydro One fixed the issue by closing a tie-breaker to reduce the grid impedance, indicating that the oscillation mode is influenced by grid impedance.

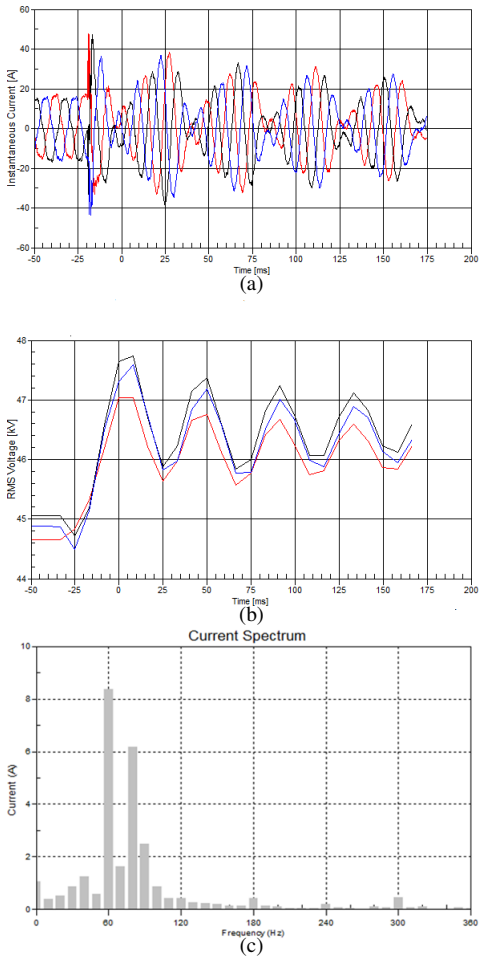


Fig. 1: (a) The recorded instantaneous current waveforms. (b) The recorded RMS voltage. (c) The current spectrum. Source: C. Li.

B. AEMO 19-Hz Oscillations

On 20th August 2020, a transmission fault resulted in a trip of a 220-kV transmission line in northwest Victoria, Australia. This resulted in several wind farms tripping. After the trip, AEMO has observed 19-Hz voltage oscillations. The oscillation was found largest at the location of solar farm was tripped, with peak-peak oscillation at around 1% (0.01 p.u. on voltage). These oscillations occurred in both real and reactive power flow from a number of IBRs connected in that area with the magnitude of oscillations ranging from as low as 0.1% to as high as 2%. Fig. 2 shows measured responses.

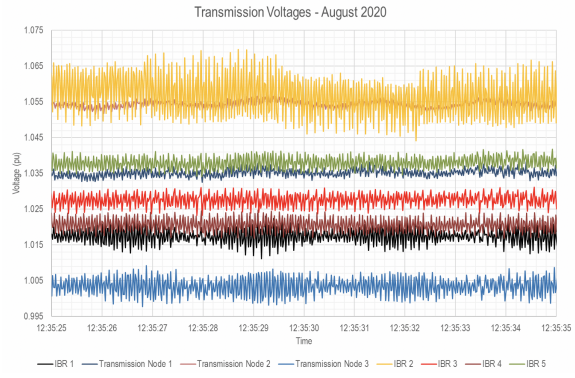


Fig. 2: AEMO 19-Hz oscillations - West Murray area. Source: AEMO.

C. Dominion Energy 22-Hz Oscillations

An oscillation mode was reported by Dominion Energy that was identified in synchrophasor data measured at solar source penetrated substations with ambient operating conditions [5]. The oscillation mode frequency was found to be 8 Hz from synchrophasor data with a 30-frame/second sampling rate, and 22 Hz from synchrophasor data with a 60-frame/second sampling rate. It can be seen that the oscillation is obvious during day time. From high frequency Point-on-Wave (PoW) measurements of phase voltage and current, the components are at 38 Hz and 82 Hz, shown in Fig. 3. Thus, in the RMS measurements, the oscillation frequency is indeed 22 Hz. Due to aliasing, the mode is identified as 8 Hz for a 30-frame/second sampling rate. It is worth noting that the oscillation is insignificant and does not affect normal operation.

© 2022 IEEE. Personal use is permitted, but republication/redistribution requires IEEE permission. See https://www.ieee.org/publications/rights/index.html for more information.
Authorized licensed use limited to: University of South Florida. Downloaded on October 29,2022 at 18:32:03 UTC from IEEE Xplore. Restrictions apply.

This article has been accepted for publication in IEEE Transactions on Energy Conversion. This is the author's version which has not been fully edited and content may change prior to final publication. Citation information: DOI 10.1109/TEC.2022.3206795

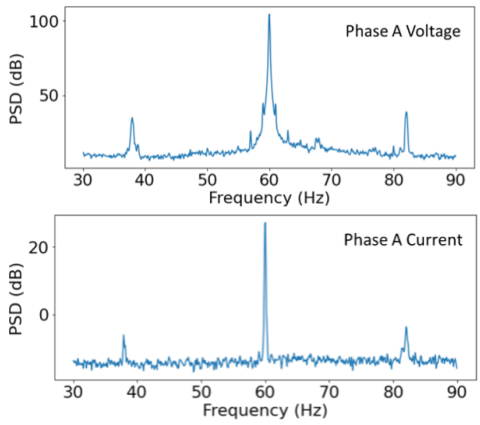


Fig. 3: Dominion Energy 22-Hz oscillations: spectrogram. Power spectral density (PSD) plots of phase voltage and current. Source: Dominion Energy.

D. Comparison of the three events

The event data and other observations show stark difference between the Hydro One event and the other two events. First, in phase current spectrums, Hydro One event shows a predominant 80 Hz component with a significant magnitude, while the other two events show two frequency components symmetric to the fundamental component (or sideband oscillations according to [11]) with insignificant magnitudes. Second, the Hydro One oscillations were obvious at low power output conditions in the early morning, while the Dominion Energy oscillations becomes visible with high power output at day time. Thus, it is concluded that the oscillations are caused by very different mechanisms.

III. The Study System and the Linear Model

A test bed is constructed and shown in Fig. 4. A 400-V VSC is used to represent the aggregated three solar PV farms, totaling 30 MW. The power base is set as 30 MVA. The solar PV is connected to the bus through a choke filter. The filter's resistance R and inductance L parameters are set as 0.015 p.u. and 0.15 p.u., respectively.

The 44-kV feeder is represented by an impedance and its complex value at the nominal frequency is $Z_{\text{feeder}} = 0.0651 + j0.1805$ p.u. This feeder is connected to a substation bus where the 29.6 MVAr shunt capacitor is connected. The substation bus is further connected to an infinite bus v_g behind a source impedance $Z_g = R_g + sL_g$. Since the fault level of the substation bus is 430 MVA, the source impedance at the nominal frequency is $0.007 + j0.0698$ p.u.. The test bed's data of the feeder, the shunt capacitor, and the grid source impedance are based on the real-world system and information from [3]. Viewed from the point of common coupling (PCC) bus, the total reactance of the grid is about 0.25 pu or the short circuit ratio (SCR) is 4 in this case.

While the grid parameters from the PCC bus to the infinite bus adhere to the real world info, the information on converters is based on assumption. The converter is assumed to have proportional resonant (PR) current control with the PCC voltage feedforward unit. Its overall control structure is shown in Fig. 4. A delay unit T_d is used to represent delays caused by pulse width modulation switching and control communication. The transfer function of the PR control is as follows.

$$\text{PR}(s) = K_p + K_r \frac{2\omega_c s}{s^2 + 2\omega_c s + \omega^2}, \tag{1}$$

where ω_c is $2\pi \times 2$ rad/s and ω is the nominal frequency at 377 rad/s. K_p and K_r are the gains of the proportional control and the resonant control units.

The outer control follows real and reactive power commands. Its proportional integral (PI) controllers are: $0.2{+}20/s$. The phase-locked-loop (PLL) consists of an abc/dq conversion block, a low-pass filter (LPF), a PI controller and an integral unit, as shown in Fig. 4. Parameters of the current control and the PLL will be given in Section IV.

A. Linear Model Derivation

In this subsection, the linear model will be derived. The derivation has two steps. In Step 1, inverter current control and the grid are modeled. In Step 2, the effect of PLL dynamics are added. The outer control's dynamics are ignored for simplicity. This assumption is also valid since compared to the current tracking dynamics (e.g., >100 Hz), the outer control bandwidth is very slow (e.g., 3 Hz). Thus, the current orders generated by the outer controls may be viewed as constants.

1) Step 1 : In Step 1, the inverter current control and delay due to PWM and digital control are modeled in detail. The delay unit can be approximated by Padé expression $T_d(s) = e^{-\tau s} = \frac{1-s\tau/2}{1+s\tau/2}$. The relationship between the current order i^*, the current measurement i, the PCC voltage v_{PCC}, and the converter voltage v can be found by the control logic. Furthermore, the relationship can also be found from circuit.

$$v = (v_{\text{PCC}} + \text{PR}(s)(i^* - i))\, T_d(s), \tag{2}$$

$$v = v_{\text{PCC}} + (R + sL)i. \tag{3}$$

Based on (2) and (3), the relationship of the PCC voltage, the current order, and the converter current can be written as the follows.

$$v_{\text{PCC}} = \underbrace{\left(\frac{T_d}{1-T_d}\text{PR}\right)}_{Z^*_{\text{PV}}} i^* - \underbrace{\left(R + sL + \frac{T_d}{1-T_d}(\text{PR} + R + sL)\right)}_{Z_{\text{PV}}} i \tag{4}$$

Eq. 4 shows that the converter can be viewed from the PCC bus as a voltage source $Z^*_{\text{PV}}(s)i^*$ behind an impedance Z_{PV}. The grid can be viewed from the PCC bus as Z_{grid}. The grid impedance consists of the feeder, the shunt capacitor, and the source impedance:

$$Z_{\text{grid}}(s) = R_{\text{feeder}} + sL_{\text{feeder}} + \frac{1}{sC + \frac{1}{R_g + sL_g}}, \text{ with shunt} \tag{5}$$

If the shunt capacitor is not included, the impedance is expressed as follows.

$$Z_{\text{grid}}(s) = R_{\text{feeder}} + sL_{\text{feeder}} + R_g + sL_g, \text{ without shunt} \tag{6}$$

© 2022 IEEE. Personal use is permitted, but republication/redistribution requires IEEE permission. See https://www.ieee.org/publications/rights/index.html for more information.
Authorized licensed use limited to: University of South Florida. Downloaded on October 29,2022 at 18:32:03 UTC from IEEE Xplore. Restrictions apply.

This article has been accepted for publication in IEEE Transactions on Energy Conversion. This is the author's version which has not been fully edited and content may change prior to final publication. Citation information: DOI 10.1109/TEC.2022.3206795

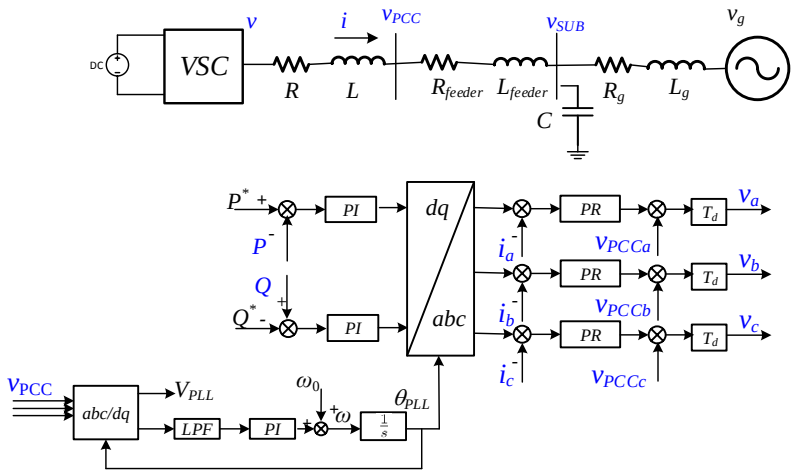


Fig. 4: The test bed circuit topology and the assumed VSC control structure. $Z_{\text{feeder}} = 0.0651 + j0.1805$ p.u. $Z_g = 0.007 + j0.0698$ p.u., $B_c = 29.6/30$ p.u.. RL choke filter: $R = 0.015$ p.u., and $L = 0.15$ p.u. Outer control: $0.2 + 20/s$.

If the grid voltage has no deviation, i.e., $v_g(s) = 0$, the current measurement can be expressed by $Z^*_{\text{PV}}(s)i^*$ only.

$$i(s) = \frac{Z^*_{\text{PV}}(s)i^* - v_g(s)}{Z_{\text{grid}}(s) + Z_{\text{PV}}(s)} = \frac{1}{Z_{\text{grid}}(s) + Z_{\text{PV}}(s)} Z^*_{\text{PV}}(s)i^*. \tag{7}$$

The PCC voltage can further be found as $Z_{\text{grid}}(s)i(s)$:

$$v_{\text{PCC}} = \underbrace{\frac{Z_{\text{grid}}(s)}{Z_{\text{grid}}(s) + Z_{\text{PV}}(s)} Z^*_{\text{PV}}(s)}_{G_1} i^*. \tag{8}$$

2) Step 2: Next, the PLL dynamics will be included. The relationship between v_{PCC} and i^* is expressed in the static frame. For the complex phasors in a dq frame with a constant rotating speed of ω_1 (notated as the grid dq frame), then the relationship is as follows by simply replacing s by $s + j\omega_1$.

$$\overline{V}_{\text{PCC}} = \underbrace{\frac{Z_{\text{grid}}(s + j\omega_1)}{Z_{\text{grid}}(s + j\omega_1) + Z_{\text{PV}}(s + j\omega_1)} Z^*_{\text{PV}}(s + j\omega_1)}_{G_{1,dq}} \overline{I}^* \tag{9}$$

For the real variables in the grid dq frame, the above expression becomes the following:

$$\begin{bmatrix} v_{\text{PCC},d} \\ v_{\text{PCC},q} \end{bmatrix} = \begin{bmatrix} G_{1R} & -G_{1I} \\ G_{1I} & G_{1R} \end{bmatrix} \begin{bmatrix} i^*_d \\ i^*_q \end{bmatrix}, \tag{10}$$

where $G_{1R} = \text{real}(G_{1,dq})$ and $G_{1I} = \text{imag}(G_{1,dq})$.

The current orders i^*_{abc} are generated from the dq-frame current orders (notated as i'^*_d and i'^*_q) after dq/abc conversion. This dq frame is based on the PLL angle ($\theta = \omega_1 t + \Delta\theta$) . The current orders i^*_{abc} can also be expressed using the current orders in the grid dq frame (notated as i^*_d and i^*_q). The grid dq frame rotates at a constant speed ω_1 and aligns with the PLL frame at the initial condition. Hence the angle of this grid dq frame is $\omega_1 t + \Delta\theta_0$, where $\Delta\theta_0$ is the initial phase angle of the PCC voltage phasor.

Note that at initial operating conditions, $i'_d = i_d$ and $i'_q = i_q$, since the two dq frames align with each other at steady state. The space vector of the current order viewed from the static frame can be expressed in two ways using the current orders expressed in the two dq frames.

$$\begin{aligned} \vec{i}^* &= (i'^*_d + ji'^*_q)e^{j(\omega_1 t + \Delta\theta)}, \text{ PLL dq frame} \\ &= (i^*_d + ji^*_q)e^{j(\omega_1 t + \Delta\theta_0)}, \text{ Grid dq frame.} \end{aligned} \tag{11}$$

Therefore,

$$i^*_d + ji^*_q = (i'^*_d + ji'^*_q)e^{j\Delta\delta} \tag{12}$$

where $\Delta\delta = \Delta\theta - \Delta\theta_0$ and $\Delta\delta$ is 0 at the initial condition. Linearizing the above equation leads to the following:

$$\begin{aligned} \Delta i^*_d &= \Delta i'^*_d - i_q \Delta\delta \\ \Delta i^*_q &= \Delta i'^*_q + i_d \Delta\delta \end{aligned} \tag{13}$$

Note that the PLL's output angle is associated with $\Delta v_{\text{PCC},q}$:

$$\Delta\delta = G_{\text{PLL}} \Delta v_{\text{PCC},q}, \tag{14}$$

where $G_{\text{PLL}} = \frac{V_{\text{PCC}}(K_p + K_i/s)/s \cdot \text{LPF}(s)}{1 + V_{\text{PCC}}(K_p + K_i/s)/s \cdot \text{LPF}(s)}$, V_{PCC} is the PCC voltage magnitude, K_p and K_i are the PI controller parameters.

The LPF's transfer function can be either first order or second order:

$$\begin{aligned} \text{LPF}(s) &= \frac{\omega_n}{s + \omega_n}, \text{ first order} \\ \text{LPF}(s) &= \frac{\omega_n^2}{s^2 + 2\zeta\omega_n s + \omega_n^2}, \text{ second order} \end{aligned}$$

If $\omega_n = 2\pi \times 25$ rad/s, the LPF will filter out high-frequency harmonics and noises above 25 Hz. ζ is the damping ratio and a typical value used is 0.707.

Remarks: The above expression relating the q-axis PCC voltage with the PLL output angle has been derived in the literature, e.g., [12], [13]. If the PCC voltage's magnitude is 1, then

$$\Delta v_{\text{PCC},q} = \Delta(V_{\text{PCC}} \sin(\Delta\delta_{\text{PCC}})) \approx \Delta\delta_{\text{PCC}},$$

where δ_{PCC} is the phase angle of the PCC voltage viewed from the grid dq frame. Therefore $G_{\text{PLL}} = \frac{\Delta\delta}{\Delta\delta_{\text{PCC}}}$ and the

© 2022 IEEE. Personal use is permitted, but republication/redistribution requires IEEE permission. See https://www.ieee.org/publications/rights/index.html for more information.
Authorized licensed use limited to: University of South Florida. Downloaded on October 29,2022 at 18:32:03 UTC from IEEE Xplore. Restrictions apply.

This article has been accepted for publication in IEEE Transactions on Energy Conversion. This is the author's version which has not been fully edited and content may change prior to final publication. Citation information: DOI 10.1109/TEC.2022.3206795

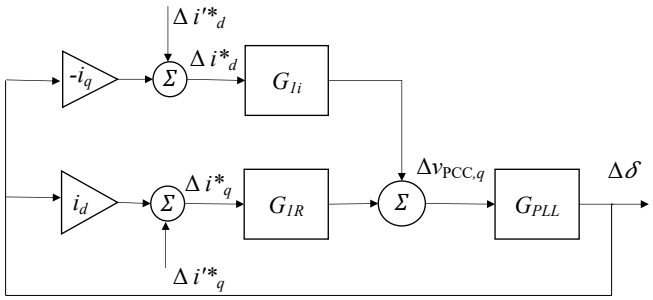


Fig. 5: Block diagram considering PLL, current control and network.

bandwidth of G_{PLL} reflects how fast a PLL can track the input angle.

B. Block diagram

With above derivation, specifically (10)(13), and (14), a block diagram can be developed to express the relationship between $\Delta\delta$, $\Delta v_{\mathrm{PCC},q}$, and the current orders, as shown in Fig. 5.

If the PV is operating at unity power factor with $Q = 0$, then $i_q = 0$. For the above system, the open-loop gain is as simple as the following:

$$OL = -i_d G_{1R} G_{\mathrm{PLL}}. \tag{15}$$

Thus, the block diagram presented in Fig. 5 can be used to examine the interaction of the PLL and the rest of the system (current control and the network).

a) A simple example: If the converter is viewed as an ideal current source $i_d^* + ji_q^*$, while the grid is viewed as pure reactance, then in the grid dq frame, the grid impedance is expressed as $Z_g = (s+j\omega_1)L_g = sL_g + jX_g$. The relationship between the the complex PCC voltage and current is expressed as:

$$\Delta\overline{V}_{\mathrm{PCC}} = Z_g(\Delta i_d^* + j\Delta i_q^*), \tag{16}$$

and the relationship between the q-axis PCC voltage and the currents can be expressed as:

$$\Delta v_{\mathrm{PCC},q} = \underbrace{X_g}_{G_{1i}} \Delta i_d^* + \underbrace{sL_g}_{G_{1R}} \Delta i_q^*. \tag{17}$$

It can be seen that G_{1R} is sX_g/ω_1.

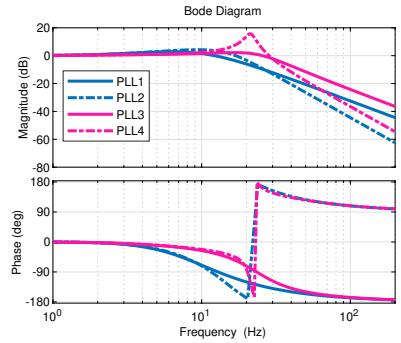
For this simple assumption, the open-loop gain is

$$OL = -i_d \cdot \frac{sX_g}{\omega_1} \cdot G_{\mathrm{PLL}}. \tag{18}$$

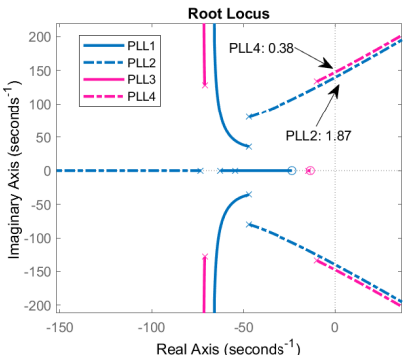
Four PLLs are examined:

- PLL1: $(K_p, K_i, \omega_n) = 60, 1400, 2\pi\times 25$ rad/s, first-order LPF. Bandwidth: 16 Hz.
- PLL2: $(K_p, K_i, \omega_n) = 60, 1400, 2\pi \times 25$ rad/s, second-order LPF. Bandwidth: 20 Hz.
- PLL3: $(K_p, K_i, \omega_n) = 150, 2000, 2\pi \times 25$ rad/s, first-order LPF. Bandwidth: 33 Hz.
- PLL4: $(K_p, K_i, \omega_n) = 150, 2000, 2\pi \times 25$ rad/s, second-order LPF. Bandwidth: 33 Hz.

The Bode plots of G_{PLL} are presented in Fig. 6(a). It can be seen that PLL4 has insufficient damping and the magnitude of G_{PLL} shows a peak at 20 Hz.



(a)



(b)

Fig. 6: (a) The Bode diagram of G_{PLL} for different parameters with first-order LPF. (b) The root locus diagram of $sG_{\mathrm{PLL}}/\omega_1$.

According to the root-locus diagram presented in Fig. 6(b), for PLL4, a fast PLL with second-order LPF, if the gain $i_d X_g$ exceeds 0.38, the system will be unstable, suffering 23-Hz oscillations. It can be clearly seen that the oscillation frequency is dependent on the poles of G_{PLL}. On the other hand, for PLL3, a fast PLL with first-order LPF, the gain margin is sufficiently large: 1.87, indicating a much stabler system.

Remarks: This simple example shows that PLL may introduce oscillations. From the system operation perspective, higher power level and weaker grid make oscillations worse. It is obvious that a PLL with a high peak gain can be subject to oscillations more easily. Note that high peak gain is not equivalent to a fast PLL with a high bandwidth. Rather, the high peak gain indicates insufficient damping. PLLs with the same bandwidth can have different peak gains.

IV. Mechanism Analysis and EMT Simulation Results

In this section, mechanism analysis and simulation results based on the EMT test bed built in MATLAB/Simscape are provided.

The following case studies have been designed to demonstrate oscillations with a frequency at 20 Hz range in RMS measurements with three distinct causes. Time-domain simulation results, as well as voltage and current spectrums, are all provided to demonstrate the signature of each type of oscillations. Furthermore, mechanism analysis is conducted by use of the linear model derived in Section III.

- Case 1: 22-Hz oscillations mainly due to the inverter current control and grid interactions.

© 2022 IEEE. Personal use is permitted, but republication/redistribution requires IEEE permission. See https://www.ieee.org/publications/rights/index.html for more information.
Authorized licensed use limited to: University of South Florida. Downloaded on October 29,2022 at 18:32:03 UTC from IEEE Xplore. Restrictions apply.

This article has been accepted for publication in IEEE Transactions on Energy Conversion. This is the author's version which has not been fully edited and content may change prior to final publication. Citation information: DOI 10.1109/TEC.2022.3206795

- Case 2: 20-Hz oscillations mainly due to insufficient damping of PLL.
- Case 3: 27-Hz oscillations mainly due to interactions of the PLL and the shunt capacitor.

A. Case 1: Slow current control and delay induced oscillations

For case 1, the current control is assumed to be slow and the PR control's transfer function is as follows.

$$\mathrm{PR}(s) = 0.35 + 2\frac{2\omega_c s}{s^2 + 2\omega_c s + \omega^2}, \text{ slow control}$$

The control delay is assumed to be 200 μs.

As a comparison, a fast control is assumed to have the following transfer function:

$$\mathrm{PR}(s) = 1 + 10\frac{2\omega_c s}{s^2 + 2\omega_c s + \omega^2}, \text{ fast control}$$

The control delay is assumed to be 100 μs.

The circuit parameters have been given in Section III and the caption of Fig. 4. For case 1, the SCR viewed from the PCC bus is 4 based on the rated power of the IBR.

The PLL's open-loop transfer function is assumed as follows:

$$G_{\mathrm{OL,PLL}} = \left(100 + \frac{2000}{s}\right)\frac{1}{s}\frac{2\pi \times 25}{s + 2\pi \times 25}.$$

Note that the first-order LPF is used for this PLL. The closed-loop system $G_{\mathrm{PLL}} = \frac{G_{\mathrm{OL,PLL}}}{1+G_{\mathrm{OL,PLL}}}$ has a pair of poles at about 13 Hz: $-47 \pm j80$.

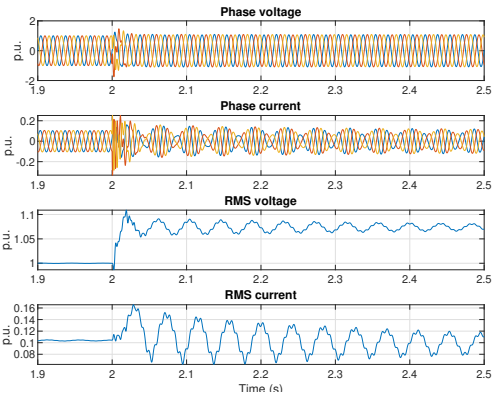
Fig. 7 presents the time-domain simulation results (three-phase PCC voltage, three-phase converter current, phase A voltage RMS measurement, phase A current RMS measurement, real power, reactive power measured at the PCC bus from the IBR, and the two outputs from PLL: voltage magnitudes and frequency) and the spectrum of the PCC bus phase voltage and phase current. The 30-MVAr shunt capacitor will be switched in at $t = 2$ s. The solar PV power exporting level is assumed at a low level: 0.1 p.u.. It can be seen that the oscillations appear when the capacitor is switched in. Furthermore, the oscillations manifest as a 22-Hz mode in the RMS voltage, current and power measurements. In the phase current and voltage, the 82-Hz component is predominant besides the fundamental component.

For mechanism analysis, we compare the frequency responses of $Z_{\mathrm{grid}} + Z_{\mathrm{PV}}$, G_1, and G_{1R} for three cases: (i) slow current control, (ii) fast current control, and (iii) slow current control when the system has no shunt compensation.

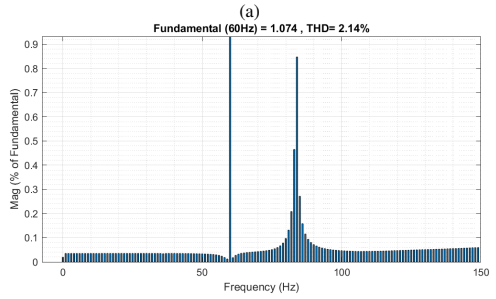
Remark: It can be seen from Fig. 8 that the shunt compensation has an insignificant impact on $Z_{\mathrm{grid}} + Z_{\mathrm{PV}}$, G_1, G_{1R}. In turn, the shunt compensation has insignificant impact on the oscillation mode.

Remark: The slow current control introduces the 20-Hz mode while the fast current control does not. When the current control is slow and the delay time is large, the equivalent impedance of the solar PV becomes much smaller, as shown in Fig. 8(a). In addition, the impedance magnitude has a dip at ~ 80 Hz approaching -20 dB, indicating a potential 80-Hz resonance in the phase currents. This dip at ~ 80 Hz in the total impedance $Z_{\mathrm{PV}} + Z_{\mathrm{grid}}$ is then manifested as the peak at 80 Hz in G_1 as shown in Fig. 8(b). This 80-Hz peak will become a peak at 20-Hz viewed from the grid dq frame. This fact can be seen by examining the frequency response of G_{1R} in Fig. 8(c).

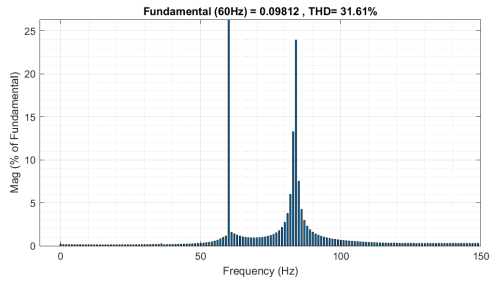
The root-locus diagram of the open-loop gain $-G_{1R}G_{\mathrm{PLL}}$



(a)



(b)



(c)

Fig. 7: Case 1. (a) Time-domain simulation results: three-phase PCC voltage, three-phase converter current, phase A voltage RMS measurement, phase A current RMS measurement, real power, reactive power measured at the PCC bus from the IBR, and the two outputs from PLL: voltage magnitude and frequency. (b) Phase voltage spectrum. (c) Phase current spectrum.

© 2022 IEEE. Personal use is permitted, but republication/redistribution requires IEEE permission. See https://www.ieee.org/publications/rights/index.html for more information.
Authorized licensed use limited to: University of South Florida. Downloaded on October 29,2022 at 18:32:03 UTC from IEEE Xplore. Restrictions apply.

This article has been accepted for publication in IEEE Transactions on Energy Conversion. This is the author's version which has not been fully edited and content may change prior to final publication. Citation information: DOI 10.1109/TEC.2022.3206795

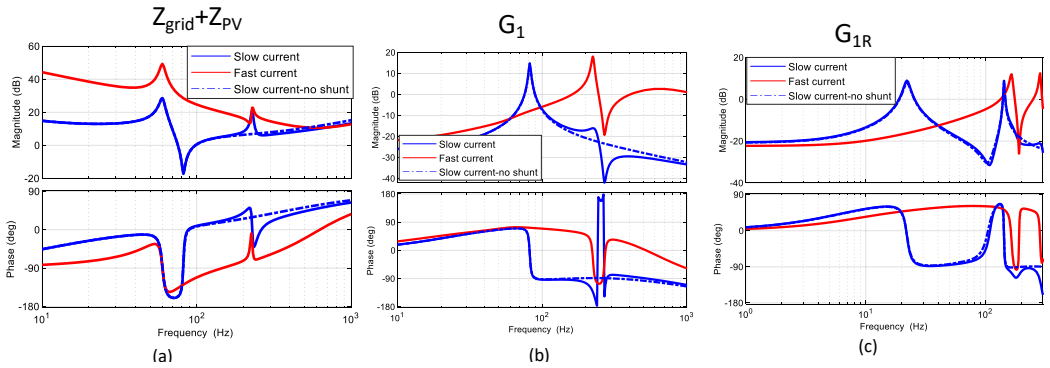


Fig. 8: Case 1: Frequency responses of $Z_{\rm grid}+Z_{\rm PV}$, G_1 and G_{1R}. A dip at 80 Hz in $Z_{\rm grid}+Z_{\rm PV}$ caused by slow current control leads to a peak at 20 Hz and a valley at 100 Hz in G_{1R}.

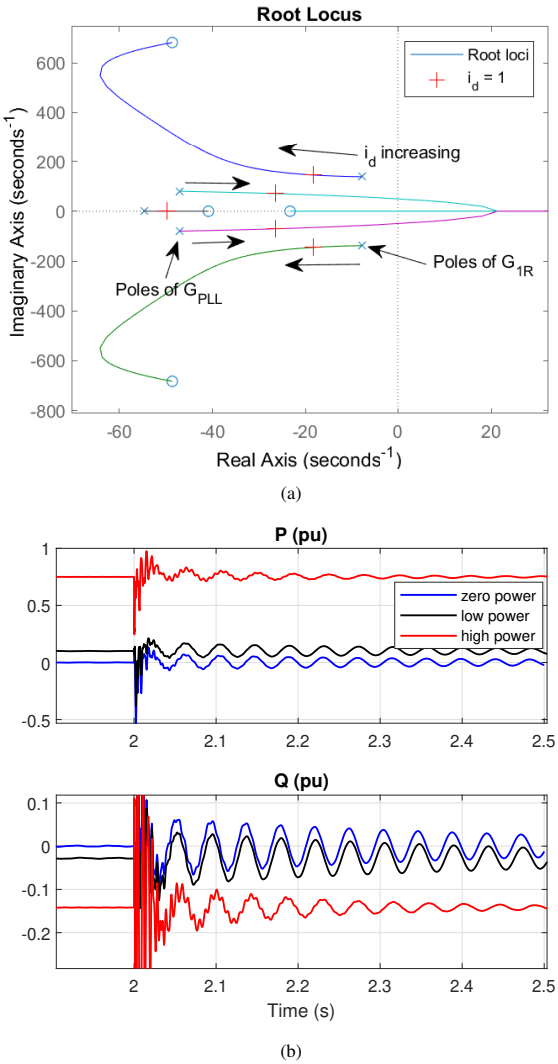


Fig. 9: (a) The root-locus diagram of $-G_{1R}G_{\rm PLL}$ shows that the dominant mode at 22 Hz moves to left when i_d or power exporting level increases. (b) EMT simulation results show oscillations are worse at zero or lower power levels.

is presented in Fig. 9(a). It can be seen that an open-loop pole at 22 Hz is moving to the left towards a zero at 100 Hz. This mode is the dominant 22 Hz mode that is created from G_{1R}'s poles. Hence, the 22-Hz oscillation mode is due to the slow current control and the large delay time constant.

In the root-locus diagram, the PLL's pole moves towards the right-half-plane (RHP) while the 22-Hz mode moves towards the left when i_d or the power exporting level increases. This point is also verified by the EMT simulation results presented in Fig. 9(b). It can be seen that the 22-Hz oscillations have more damping if the power exporting level increases.

The 20-Hz oscillations observed in Hydro One solar PVs have a very similar feature as the 22-Hz oscillations demonstrated in Case 1.

1) The 80-Hz component in the Hydro One oscillations is dominant in the phase current and the magnitude of this component is significant compared to the magnitude of the fundamental component. Same is true for the Case 1 oscillations that 82-Hz component is dominant.
2) The oscillations are worse if the solar PV exporting power level is low. Same is true for the Case 1 oscillations.

B. Case 2: Insufficient damping of PLL

The circuit parameters and the grid strength of Case 2 are the same as those of Case 1. The SCR viewed at the PCC bus is 4. For inverter current control, the fast current control and a small control delay time constant at 50 μs are assumed. The PLL's open-loop transfer function is assumed as follows:

$$G_{\rm OL,PLL}=\left(150+\frac{3000}{s}\right)\frac{1}{s}\frac{\omega_n^2}{s^2+2\zeta\omega_n s+\omega_n^2}. \qquad (19)$$

where $\omega_n=2\pi\times 25$ rad/s and $\zeta=0.707$. Note that in Case 2, the LPF is assumed to be second order. The closed-loop system $G_{\rm PLL}$ has a pair of poles: $-7\pm j132$.

Fig. 10 presents the EMT simulation results upon switching in the shunt capacitor and the spectrums of the phase voltage and current. It can be seen that the system shows 20-Hz oscillations in the RMS voltage, current, and power measurements. In RMS voltage, the peak to peak magnitude of the oscillation is very small, less than 1% p.u.. The current and voltage spectrums show that there are both 40-Hz and 80-Hz components.

For mechanism analysis, frequency responses of the system with different PLLs are compared in Fig. 11(a). Fast PLL

© 2022 IEEE. Personal use is permitted, but republication/redistribution requires IEEE permission. See https://www.ieee.org/publications/rights/index.html for more information.
Authorized licensed use limited to: University of South Florida. Downloaded on October 29,2022 at 18:32:03 UTC from IEEE Xplore. Restrictions apply.

This article has been accepted for publication in IEEE Transactions on Energy Conversion. This is the author's version which has not been fully edited and content may change prior to final publication. Citation information: DOI 10.1109/TEC.2022.3206795

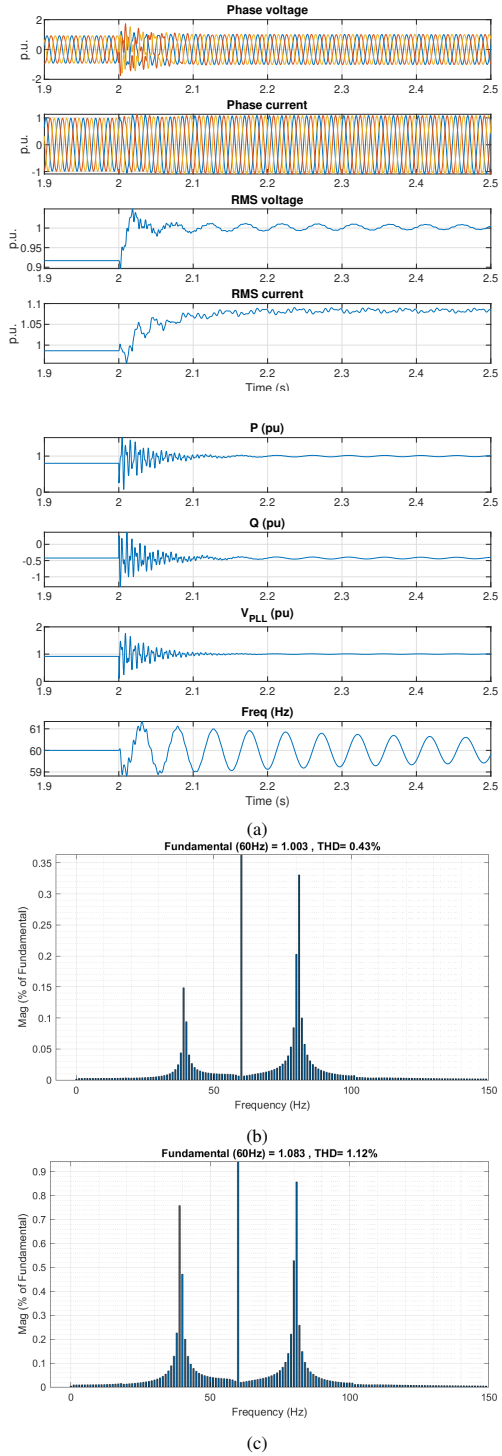


Fig. 10: Case 2. a) Time-domain simulation results: three-phase PCC voltage, three-phase converter current, phase A voltage RMS measurement, phase A current RMS measurement, real power, reactive power measured at the PCC bus from the IBR, and the two outputs from PLL: voltage magnitude and frequency. (b) Phase voltage spectrum. (c) Phase current spectrum.

refers to the PLL presented in (19). Slow PLL refers to a PLL with 60 and 1400 as its PI controller gains. Both PLLs have the same second-order LPF.

The root locus diagram of the open-loop gain $-G_{1R}G_{\text{PLL}}$ is presented to examine the effect of i_d or power level on the oscillation mode Fig. 11(b). It can be seen that fast PLL

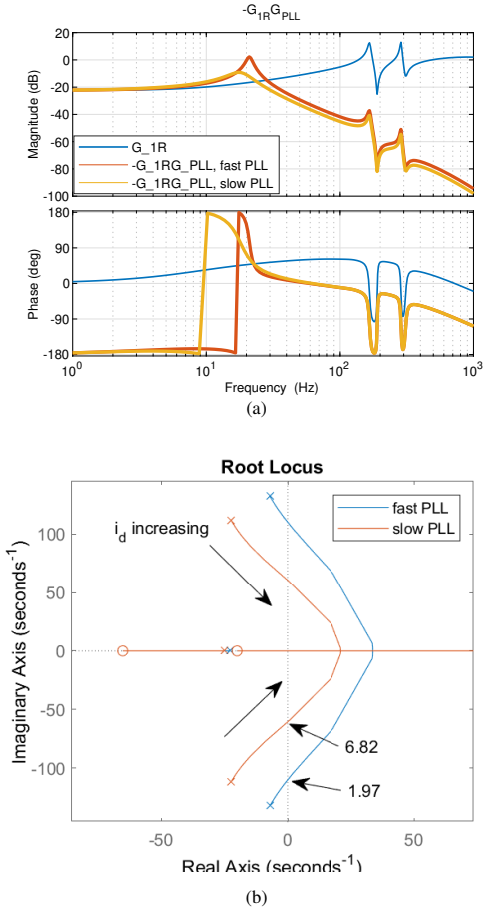


Fig. 11: Case 2. (a) The Bode diagram of $-G_{1R}G_{\text{PLL}}$ shows that fast PLL introduces a peak at 20 Hz in the dq frame. (b) The Root-Locus diagram of $-G_{1R}G_{\text{PLL}}$ shows that the fast PLL makes the system prone to oscillations and the oscillation mode is related to PLL.

introduces a peak in the open-loop gain at 20 Hz in the dq frame. Fast PLL also makes the oscillation mode originated from the pole of G_{PLL} prone to instability compared to slow PLL.

Remarks: The PLL induced oscillations have the following features.

- First, in phase current and voltage spectrum, the magnitudes of the 40-Hz and 80-Hz components are comparable. This feature indicates that the oscillation mode originates from control loops implemented in the dq frame. The 20-Hz oscillations modulate the dq-frame currents. The effect is similar as amplitude modulation in communication. Amplitude modulation with a frequency f on a carrier waveform of 60 Hz introduces $(60 + f)$ Hz and $(60 - f)$ Hz sideband oscillation modes. Thus, the 20-Hz in the dq-frame corresponds to the 40-Hz and 80-Hz components in the static frame.
- For this type of oscillations, increasing power transfer will make the oscillations worse, as indicated from the root-locus diagram in Fig. 11(b). This feature is different from Case 1. In Case 1, increasing power transfer can make the oscillations originated from G_{1R} better.
- The type of oscillations may be viewed as power quality

© 2022 IEEE. Personal use is permitted, but republication/redistribution requires IEEE permission. See https://www.ieee.org/publications/rights/index.html for more information.
Authorized licensed use limited to: University of South Florida. Downloaded on October 29,2022 at 18:32:03 UTC from IEEE Xplore. Restrictions apply.

This article has been accepted for publication in IEEE Transactions on Energy Conversion. This is the author's version which has not been fully edited and content may change prior to final publication. Citation information: DOI 10.1109/TEC.2022.3206795

issue since the peak to peak magnitude of the oscillation is very small. The spectrum analysis shows that the total harmonic distortion is 1.12% in phase current and 0.43% in phase voltage.

- Stability can be improved by tuning the PLL parameters. Replacing the second-order LPF by the first-order LPF can reduce the peak in the open-loop gain, and hence improve stability.

C. Case 3: Interactions of PLL and shunt compensation

In Case 3, we investigate a PLL with sufficient damping and its interaction with the shunt compensation. In the testbed, there are two transmission lines connecting the substation bus to the grid. The equivalent impedance $Z_g = R_g + jX_g$ where $X_g = 0.15$ p.u. and $R_g = X_g/8$. At $t = 2$ s, one of the transmission line tripped and the equivalent Thevenin impedance of the grid is now $X_g = 0.37$. The impedance of the feeder connecting the solar PV PCC bus to the substation bus is 0.18 p.u. Viewed from the PCC bus, the SCR is approximately 1.8 after the line tripping event. Compared to Case 1 and Case 2 where the SCR at the PCC bus is 4, Case 3 is a weak grid case.

For Case 3, fast current control, 50 μs delay, first-order LPF-based PLL are adopted.

Fig. 12 presents the simulation results. It can be seen that the system's real power, reactive power, RMS measurements, and frequency are subject to 27-Hz oscillations. The phase current and voltage have both 87-Hz and 33-Hz components.

The 27-Hz oscillations in RMS measurements will not appear if the shunt compensation is not included. Fig. 13 shows the EMT simulation results with and without shunt compensation. It is clear that without shunt compensation, there are no oscillations after line tripping.

Therefore, it can be seen that shunt compensation does play a role in the oscillations. Comparison has been made on the frequency-domain responses of $Z_{\text{grid}} + Z_{\text{PV}}$, G_1, and G_{1R}, as shown in Fig. 14. It can be seen that the shunt compensation can significantly change G_{1R}'s frequency response. In the static frame, it can be seen that a slight change occurs at 100 Hz in $Z_{\text{grid}} + Z_{\text{PV}}$ and a peak at 100 Hz is introduced in G_1.

This 100-Hz mode is closely related to the grid impedance. As we can see from Fig. 8(b), when SCR is 4, the peak of G_1 if fast current control is implemented is located at 200 Hz above. In turn, the peak in G_{1R} will be at the frequency region of 140 Hz. Since the PLL's bandwidth is in the region of 20 Hz, when the SCR is 4, we expect insignificant interaction between PLL and G_{1R}.

However, when the grid becomes weak with SCR at 1.8, the peak in G_1 is now located at 100 Hz in the static frame, and a peak at 40 Hz is introduced in G_{1R}. The interaction of G_{1R} and G_{PLL} then introduces oscillations at the 20 Hz region, as shown in the root-locus diagram in Fig. 15. An open-loop pole associated with the PLL is moving to the RHP, while the open-loop pole associated with G_{1R} is moving to the left, when the power transfer level increases. This type of interactions has been termed as "modal resonance" in the literature, e.g., [14].

Remarks: In Case 3, the shunt compensation plays a significant role in destabilizing this mode. Without shunt, G_1 does not have a large peak at the 100-Hz region and G_{1R} does not have a large peak at 40-Hz region. With shunt, G_{1R} has a large peak at 100 Hz and a valley at 100 Hz, implicating the introduction of an open-loop pole at 40 Hz and an open-loop zero at 100 Hz.

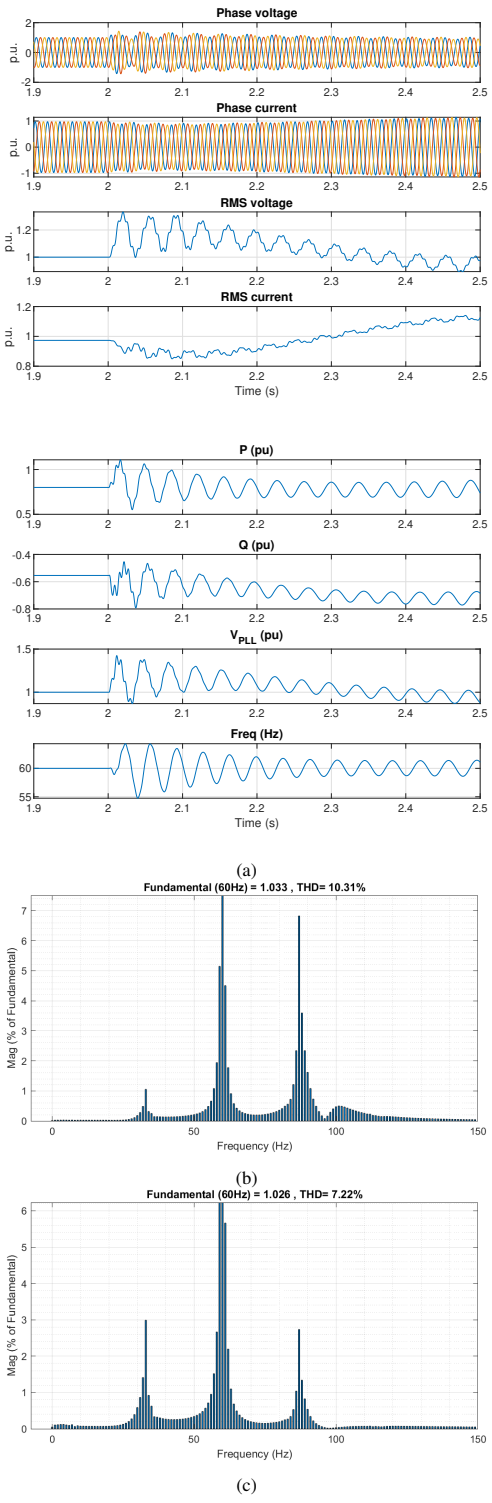


Fig. 12: Case 3. a) Time-domain simulation results: three-phase PCC voltage, three-phase converter current, phase A voltage RMS measurement, phase A current RMS measurement, real power, reactive power measured at the PCC bus from the IBR, and the two outputs from PLL: voltage magnitude and frequency. (b) Phase voltage spectrum. (c) Phase current spectrum.

© 2022 IEEE. Personal use is permitted, but republication/redistribution requires IEEE permission. See https://www.ieee.org/publications/rights/index.html for more information.
Authorized licensed use limited to: University of South Florida. Downloaded on October 29,2022 at 18:32:03 UTC from IEEE Xplore. Restrictions apply.

This article has been accepted for publication in IEEE Transactions on Energy Conversion. This is the author's version which has not been fully edited and content may change prior to final publication. Citation information: DOI 10.1109/TEC.2022.3206795

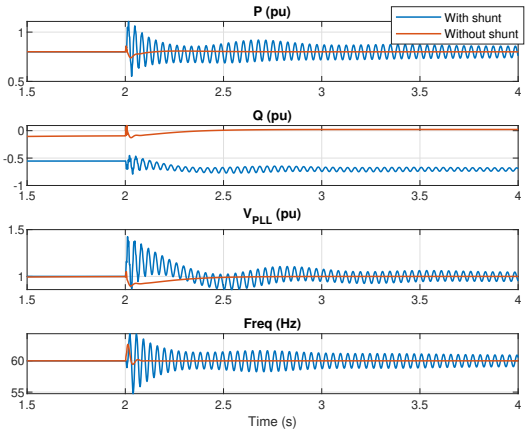


Fig. 13: Case 3: Comparison of EMT simulation results for a system with or without shunt. X_g increases to 0.37 p.u. at $t = 2$ s. If there is no shunt compensation, the system will not experience oscillations at this condition.

Based on the root-locus diagram of $-G_{\rm PLL}G_{1R}$, without shunt, the marginal gain is 3.31. That is, i_d has to increase to 3.31 to make the system unstable. With shunt, the marginal gain reduces to 1.18.

From the root locus diagram, it can be seen that there are two loci, one starting from the pole of the PLL, moving towards right; and the other starting from the pole of G_{1R}, moving towards left. The two loci attract to each other, making the pole of the PLL move to the RHP in a much faster speed, compared to the case when the system has no shunt compensation.

Remarks: Compared to Case 2, the oscillations are the result of the interaction of the PLL and shunt compensation. It is discovered that shunt compensation can play a significant role in creating oscillations. For this type of oscillations, increasing power transfer or reducing the grid strength can make the oscillation worse.

Remarks: In both Case 2 and Case 3, two frequency components with comparison magnitudes appear in the current spectrum. A close examination shows that Case 3 oscillations can lead to more than 10% voltage magnitude oscillations. On the other hand, the Case 2 oscillations lead to about 1% voltage and current magnitude oscillation.

Both the Dominion Energy 22-Hz oscillations and the AEMO 19-Hz oscillations have very small magnitudes in voltage. Based on the limited comparison cases provided in this paper, the AEMO 19-Hz oscillations and Dominion Energy 22-Hz oscillations are more aligned to the Case 2 oscillations induced by the PLL. This speculation is by no means definite. Further analysis is necessary since the EMT model used in this paper has not included limits in the PLL. According to [15], PLLs may have frequency limiters. And according to [16], PLLs may have frequency slope limiters. Those limiters will all influence the dynamic behavior. Furthermore, in the outer control, real power regulation is assumed in the current paper. It is well known that dc-link voltage control leads to a higher bandwidth of the outer control and may interact with PLL [7]. Many more analyses will be needed to develop better

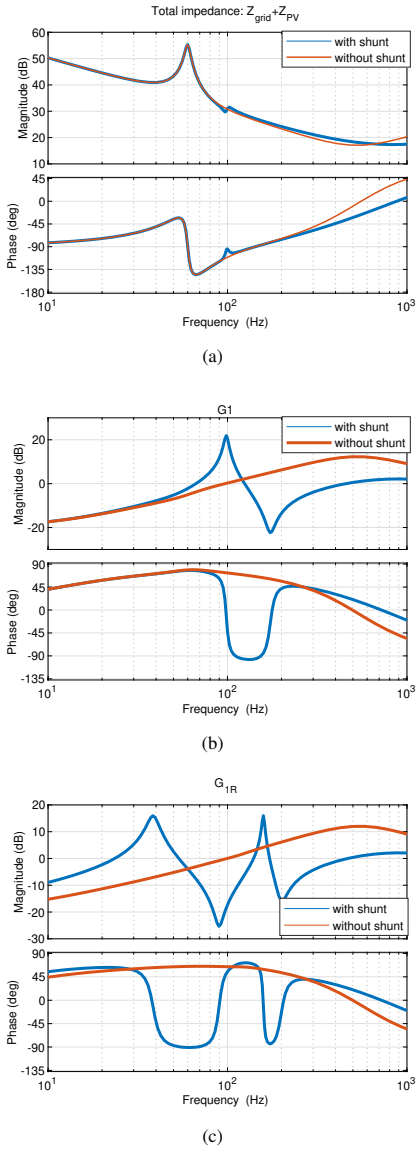


Fig. 14: Case 3: Frequency response comparison. (a) $Z_{\rm grid} + Z_{\rm PV}$ viewed from the static frame. (b) G_1 viewed from the static frame. (c) G_{1R} viewed from the dq frame.

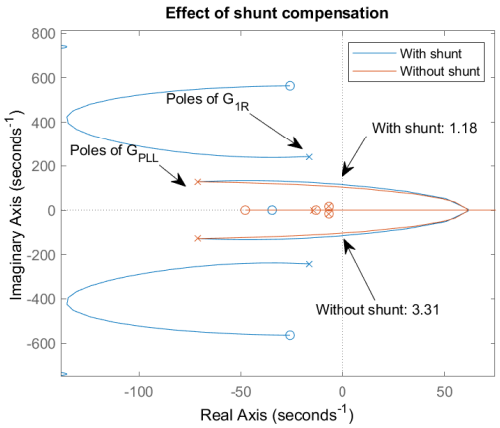


Fig. 15: Case 3: Root loci of $-G_{1R}G_{\rm PLL}$ with or without shunt compensation.

© 2022 IEEE. Personal use is permitted, but republication/redistribution requires IEEE permission. See https://www.ieee.org/publications/rights/index.html for more information.
Authorized licensed use limited to: University of South Florida. Downloaded on October 29,2022 at 18:32:03 UTC from IEEE Xplore. Restrictions apply.

This article has been accepted for publication in IEEE Transactions on Energy Conversion. This is the author's version which has not been fully edited and content may change prior to final publication. Citation information: DOI 10.1109/TEC.2022.3206795

speculation.

D. Discussion on signatures

a) Large or small voltage oscillations: The comparison conducted for three causations (slow current control, PLL with insufficient damping, interactions of PLL and shunt compensation) shows that if the the PLL is the only contributor, the oscillation magnitudes in voltage and current are small. Otherwise, if the electric circuit and current control also engage in contributing to the oscillation mode, oscillations in voltage and current become more severe. For Case 1 and Case 3, where the electric network is engaged in creating the oscillation, G_{1R}, which represents the electric circuit and current control effects, has a large peak at the 20 Hz–40 Hz in its magnitude. This is not the case for Case 2 where G_{1R} has a small magnitude at $\sim$ 20 Hz region. Therefore, in Case 1 and Case 3, we expect to see the PCC voltage will have larger oscillation magnitudes compared to Case 2.

b) Sideband oscillations or one-side dominant oscillations: Comparison shows that if the PLL is the main contributor of the oscillation mode, sideband oscillations will appear in the phase current spectrum. If the current control is the main contributor, a supersynchronous mode is dominant in the phase current spectrum.

c) Influence of power exporting level : If slow current control is the main contributor of oscillations, lower power export makes oscillations worse. If the PLL is the main contributor, higher power export makes oscillations worse.

These findings may also be applicable to a GFL with dq-frame-based proportional integral (PI) current control. For example, a popularly cited paper [17] indicates that PLL with a high bandwidth may cause oscillations. The inverter has PI current control implemented in the dq frame. Ref. [18] indicates that lack of damping in PLL may cause oscillations The GFL structure studied in that letter has PI current control implemented in the dq frame.

V. Conclusions

In this work, we examined three real-world events related to solar PV subsynchronous oscillations at 20 Hz. Using a test bed of a single IBR grid integrated system with shunt compensation modeled, we find three possible causes of oscillations at 20 Hz: slow current control (Case 1), PLL with insufficient damping (Case 2), interaction of PLL and shunt compensation (Case 3). Signatures from measurement data of the Hydro One 20-Hz oscillations align with the signatures of the Case 1 oscillations, while the signatures of the AEMO and Dominion Energy oscillations are more aligned to Case 2. Further studies are necessary to examine the effect of many other elements, e.g., PLL limiters, fast outer controls, etc.

Acknowledgement

The authors wish to acknowledge Kemal Celik, project manager of DE-EE-0008771 for his encouragement and recognition of this work. The authors wish to acknowledge Dr. Chester Li for many insightful and thought provoking discussions, Dr. Jan Shair for providing editorial suggestions, and anonymous reviewers and editor for providing valuable feedback.

References

[1] D. Shu, X. Xie, H. Rao, X. Gao, Q. Jiang, and Y. Huang, "Sub- and super-synchronous interactions between statcoms and weak ac/dc transmissions with series compensations," *IEEE Transactions on Power Electronics*, vol. 33, no. 9, pp. 7424–7437, 2017.

[2] N. Hatziargyriou, J. Milanovic, C. Rahmann, V. Ajjarapu, C. Canizares, I. Erlich, D. Hill, I. Hiskens, I. Kamwa, B. Pal *et al.*, "Definition and classification of power system stability revisited & extended," *IEEE Transactions on Power Systems*, 2020.

[3] C. Li, "Unstable operation of photovoltaic inverter from field experiences," *IEEE Transactions on Power Delivery*, vol. 33, no. 2, pp. 1013–1015, 2017.

[4] AEMO, "System strength workshop," https://aemo.com.au/en/learn/energy-explained/system-strength-workshop.

[5] C. Wang, C. Mishra, and K. Jones, "Identifying oscillations injected by inverter-based solar energy sources in dominion energy's service territory using synchrophasor data and point-on-wave data," https://naspi.org/sites/default/files/2021-04/D1S1_02_wang_dominion_naspi_20210413.pdf.

[6] Y. Cheng, L. Fan, J. Rose, F. Huang, J. Schmall, X. Wang, X. Xie, J. Shair, J. Ramamurthy, N. Modi *et al.*, "Real-world subsynchronous oscillation events in power grids with high penetrations of inverter-based resources," *IEEE Transactions on Power Systems*, 2022.

[7] Y. Huang, X. Yuan, J. Hu, and P. Zhou, "Modeling of vsc connected to weak grid for stability analysis of dc-link voltage control," *IEEE Journal of Emerging and Selected Topics in Power Electronics*, vol. 3, no. 4, pp. 1193–1204, 2015.

[8] X. Wang, L. Harnefors, and F. Blaabjerg, "Unified impedance model of grid-connected voltage-source converters," *IEEE Transactions on Power Electronics*, vol. 33, no. 2, pp. 1775–1787, 2017.

[9] L. Fan, "Modeling type-4 wind in weak grids," *IEEE Transactions on Sustainable Energy*, vol. 10, no. 2, pp. 853–864, 2018.

[10] S.-H. Huang, J. Schmall, J. Conto, J. Adams, Y. Zhang, and C. Carter, "Voltage control challenges on weak grids with high penetration of wind generation: Ercot experience," in *2012 IEEE Power and Energy Society General Meeting*. IEEE, 2012, pp. 1–7.

[11] X. Wang, M. G. Taul, H. Wu, Y. Liao, F. Blaabjerg, and L. Harnefors, "Grid-synchronization stability of converter-based resources—an overview," *IEEE Open Journal of Industry Applications*, vol. 1, pp. 115–134, 2020.

[12] Z.-X. Zou and M. Liserre, "Modeling phase-locked loop-based synchronization in grid-interfaced converters," *IEEE Transactions on Energy Conversion*, vol. 35, no. 1, pp. 394–404, 2019.

[13] L. Fan, Z. Miao, and M. Zhang, "Subcycle overvoltage dynamics in solar pvs," *IEEE Transactions on Power Delivery*, vol. 36, no. 3, pp. 1847–1858, 2020.

[14] I. Dobson, J. Zhang, S. Greene, H. Engdahl, and P. W. Sauer, "Is strong modal resonance a precursor to power system oscillations?" *IEEE Transactions on Circuits and Systems I: Fundamental Theory and Applications*, vol. 48, no. 3, pp. 340–349, 2001.

[15] J. Chen, M. Liu, H. Geng, T. O'Donnell, and F. Milano, "Impact of pll frequency limiter on synchronization stability of grid feeding converter," *IEEE Transactions on Power Systems*, vol. 37, no. 3, pp. 2487–2490, 2022.

[16] M. Mirhosseini, J. Pou, V. G. Agelidis, E. Robles, and S. Ceballos, "A three-phase frequency-adaptive phase-locked loop for independent single-phase operation," *IEEE Transactions on Power Electronics*, vol. 29, no. 12, pp. 6255–6259, 2014.

[17] L. Harnefors, M. Bongiorno, and S. Lundberg, "Input-admittance calculation and shaping for controlled voltage-source converters," *IEEE transactions on industrial electronics*, vol. 54, no. 6, pp. 3323–3334, 2007.

[18] C. Li, S. Wang, and J. Liang, "Tuning method of a grid-following converter for the extremely-weak-grid connection," *IEEE Transactions on Power Systems*, pp. 1–1, 2022.

© 2022 IEEE. Personal use is permitted, but republication/redistribution requires IEEE permission. See https://www.ieee.org/publications/rights/index.html for more information.
Authorized licensed use limited to: University of South Florida. Downloaded on October 29,2022 at 18:32:03 UTC from IEEE Xplore. Restrictions apply.